Journal of Energy Storage 151 (2026) 120543

Contents lists available at ScienceDirect

Journal of Energy Storage

journal homepage: www.elsevier.com/locate/est

Research papers

Efficient structure optimization of downhole thermal management system via transfer learning surrogate modeling

Siqi Zhang, Chao Deng, Fulong Wei, Jiacheng Li, Xiaobing Luo *, Jinlong Ma *

School of Energy and Power Engineering, Huazhong University of Science and Technology, Wuhan, 430074, China

ARTICLE INFO

Keywords:
Downhole thermal management
Transfer learning
Thermal optimization
Surrogate model
Thermal resistance network
Numerical simulation

ABSTRACT

Optimizing downhole thermal management systems (DTMS) for extreme environments is a computationally intensive challenge. Traditional simulation-based optimization is prohibitively expensive, while surrogate models struggle to balance data requirements and accuracy. This study proposes a novel structural optimization framework employing a transfer learning neural network (TLNN) surrogate model. By integrating extensive low-fidelity data from a thermal resistance network with limited high-fidelity 3D simulation data, the TLNN achieves high prediction accuracy (RMSE < 1 °C) while reducing high-fidelity data requirements by over 50%. Coupled with a Genetic Algorithm (GA), the framework reduces computational cost by 62% compared to conventional methods, effectively avoiding local optima traps. The optimized DTMS design successfully maintains electronics below 160 °C for 18 h in a 225 °C environment, offering an efficient solution for complex thermal system design.

1. Introduction

The exploration and development of oil and gas resources are advancing toward deeper and more geologically complex formations due to the exhaustion of shallow oil and gas resources [1–4]. Logging tools play a critical role in downhole formation evaluation, integrating a variety of electronic components to acquire and transmit geophysical data in real time [5–7]. However, in ultra-deep reservoirs, logging tools are routinely exposed to extreme temperatures that can exceed 200 °C [8–10], which presents a severe challenge to the temperature reliability of downhole electronics [11,12]. Developing high-temperature-resistant electronic devices is a potential solution, but it remains technically demanding and costly, often failing to keep pace with the urgent requirements of practical applications [13–15].

To ensure the stable operation of downhole electronics in high-temperature environments, DTMS have been developed as an integral subsystem of modern logging tools. Passive DTMS are widely adopted for their simplicity, reliability, and independence from external energy [16,17]. The core principle of the system involves the use of vacuum insulation and composite thermal insulators to isolate heat intrusion while integrating PCM-based heat sinks to absorb and store heat generation [18–21]. This setup effectively provides long-term protection for electronics under extreme conditions, positioning them as the dominant solution in industrial logging applications [22,23].

For large and multifunctional logging tools, such as nuclear magnetic resonance and sidewall coring instruments, the incorporation of numerous electronics necessitates sophisticated designs for their DTMS. A distributed DTMS configuration, whose advantages were investigated and validated by Lan et al. [24], represents an effective strategy for managing the complex thermal loads in these tools. In this setup, electronic devices are individually mounted on separate skeletons, with heat sinks placed between them to manage thermal loads at multiple points along the tool axis. Indeed, building upon such an architecture, Peng et al. [25] developed a durable DTMS for a sidewall coring tool, which enabled prolonged operation in extreme environments. While these distributed DTMS solutions signify considerable advancements in extending the operational limits of downhole instruments, a specific opportunity remains for further enhancing their thermal performance through rigorous structural optimization. The systematic application of advanced optimization techniques holds the promise of not only minimizing the operating temperatures of electronic devices but also reducing computational design costs.

Achieving the optimal structural design for a DTMS necessitates a thorough evaluation of the relationship between the structural variables and optimization objectives. Given the considerable expense and practical limitations of extensive experiments, numerical simulation has emerged as the cornerstone for assessing DTMS thermal performance. Heat transfer models of varying computational dimensionality have been developed, ranging from rapid 1D prediction models [26] to 2D

* Corresponding authors.
E-mail addresses: luoxb@hust.edu.cn (X. Luo), majinlong@hust.edu.cn (J. Ma).

https://doi.org/10.1016/j.est.2026.120543
Received 14 September 2025; Received in revised form 24 December 2025; Accepted 12 January 2026

Nomenclature

ρ	density
c	specific heat capacity
k	thermal conductivity
T	temperature
t	time min
Q	power per unit volume
r_h	radius of the wellbore wall
r_t	radius of the logging tool
α_{mud}	thermal diffusion coefficient of drilling mud
L	length of the tool
R_f	radius of the flask wall
R_t	radius of the skeleton
Pr	Prandtl number
k_{eff}	equivalent thermal conductivity
A	surface area
θ	volume fraction of liquid phase
L_{pcm}	latent heat
M_{pcm}	mass fraction
C	equivalent nodal heat capacity
R	thermal resistance
$\mathscr{L}$	error of output layer
ψ	neuron network parameter
η	learning rate
y	simulation result
$\widehat{y}$	prediction result

Subscripts

solid	solid phase of PCMs
liquid	liquid phase of PCMs
pcm	PCM
i	node i
j	node j
p	radial layer p

Abbreviations

DTMS	downhole thermal management system
FEM	finite element method
NM	Nelder-Mead
PCM	phase change material
LMPA	low melting point alloy
TLNN	transfer learning neuron network
TRN	thermal resistance network
GA	genetic algorithm
ANN	artificial neural network
LHS	Latin hypercube sampling
RMSE	root mean square error

axisymmetric models [23] and full 3D FEM models [27]. Among these, 3D numerical models provide the most accurate evaluation results by comprehensively simulating the intricate heat transfer processes—including conduction, convection, and radiation—within the DTMS. For instance, Peng et al. [28] proposed such a 3D numerical model that achieved an average temperature error of only 3.02 °C, underscoring its high accuracy. Consequently, researchers have combined accurate 3D models with intelligent algorithms for DTMS structural optimization. For example, Zhang et al. [29] significantly reduced the maximum temperature of the heat sources in a compact DTMS through structure optimization using 3D simulation integrated with the NM algorithm.

However, these direct simulation-based optimization methods encounter significant challenges. Primarily, FEM-based optimization frameworks require dozens of iterations for DTMS optimization [29]. Considering that a single high-fidelity 3D numerical simulation can take several hours to complete [26], the entire design cycle is substantially prolonged. Furthermore, commonly employed optimization algorithms like the NM algorithm, while efficient per iteration, are prone to premature convergence to local optima [30]. This susceptibility necessitates careful initialization and repeated trial-and-error, greatly reducing the efficiency of optimal design. Regarding the local optima issue, Wei et al. [31] attempted to utilize GA for global optimization, but were also stymied by the computational cost of numerous 3D simulations and did not achieve the desired optimization effect. Current approaches often employ a surrogate model-based optimization framework, utilizing data-driven surrogate models to replace expensive 3D simulations [32–34]. Typically, this method involves generating samples of 3D simulation results within the defined design domain and fitting a surrogate model, such as Kriging model [35] or ANN [36]. Nevertheless, for DTMS characterized by complex structures and intricate heat transfer processes, a critical challenge in surrogate model construction exists: achieving an optimal trade-off between predictive accuracy and the computational cost associated with generating sufficient high-fidelity data [37].

To address the challenge of constructing accurate surrogate models with minimal computational resources, this study introduces a novel multi-fidelity surrogate modeling method based on TLNN. The principle of transfer learning, which has been successfully applied in aerodynamic shape optimization by Wu et al. [38], involves an initial phase where a model learns general patterns from a large foundational dataset. The pre-trained knowledge is then transferred to a specific domain, where the model is fine-tuned using a small number of domain-specific samples to achieve accurate predictions [39]. For the thermal optimization problem in this paper, the TRN model of DTMS is established to efficiently obtain the foundational sample data required by the TLNN. Conceptually, since the TRN model is based on the physical processes of heat transfer, its generated low-fidelity samples enable the neural network to first learn the fundamental physical skeleton of heat conduction. Subsequently, only a few high-fidelity 3D samples are required to fine-tune the model, allowing it to capture the complex fidelity details (e.g., local 3D effects). This two-stage strategy ensures both physical consistency and high prediction accuracy.

In the following, the effectiveness of the proposed TLNN-based surrogate model optimization framework for DTMS structural optimization was validated. Compared to traditional methods, the proposed approach demonstrated superior accuracy with the same computational resources. The surrogate model was integrated into a GA loop to optimize the lengths of insulators and heat sinks in DTMS. During optimization, the local optima issue presented in previous studies was identified and resolved. Results revealed significant thermal performance improvement and substantial reduction in computational cost for optimization. Furthermore, leveraging the efficiency of the framework, we explored optimal DTMS structures under various operating conditions.

2. Geometry and model

2.1. System geometry and design parameters

Fig. 1 shows the structure of the DTMS employed in a logging tool. During operation, the tool is subjected to ambient temperatures exceeding 200 °C. To protect the downhole electronics from the extreme environment, the vacuum flask is utilized as the electronics chamber, which is fabricated from high-strength metal. The vacuum cavity between its inner and outer walls provides effective radial thermal insulation. To reduce the axial heat flow, insulator 1 and insulator 2,

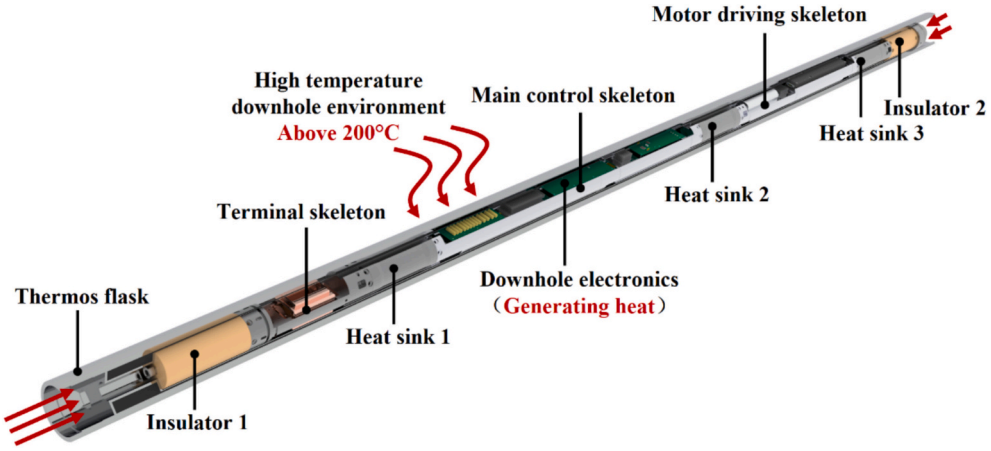

Fig. 1. Structure of the DTMS employed in a logging tool.

consisting of PEEK shells and aluminum silicate cotton filler, are installed at each end. The required electronic devices are mounted on aluminum alloy skeletons, which are categorized by function into the terminal skeleton, main control skeleton and motor driving skeleton. Three heat sinks are arranged between the modules. The heat sinks consist of stainless-steel containers and PCMs, which are a kind of LMPA. The generated heat is absorbed and stored by heat sinks via phase transition during high-temperature operation.

Fig. 2 illustrates the heat sources distribution and geometric design variables of the DTMS. Ten discrete power electronic devices are mounted on the front and back surfaces of the three skeletons. These heat sources are sequentially designated as heat source 1 to heat source 10 in the axial progression of the assembly. Note that heat source 8 is embedded inside the skeleton, a transparent back view is provided at its location for clarity.

The thermal performance of the DTMS is significantly impacted by the non-uniform spatial distribution and varying power of its internal heat sources, necessitating that the lengths of individual heat sinks be optimized according to local thermal loads to enhance overall efficiency. A critical design trade-off exists: extending heat sink lengths improves thermal storage capacity, while increasing insulator lengths enhances thermal insulation, yet both strategies aim to reduce the operating temperatures of the downhole electronics. This balance is further constrained by dimensional restrictions from operational requirements and predefined skeleton geometry, which mandate a fixed total length for the logging tool. Therefore, the optimization focuses on determining the optimal individual lengths of two insulators (L_1, L_5) and three heat sinks (L_2, L_3, L_4), with the total length of these five components remaining constant.

2.2. Heat transfer model

In this section, heat transfer models of the DTMS are developed for analysis and optimization. For the downhole operation of the logging tool, multiple heat transfer processes are involved, such as the convective heat exchange between the drilling fluid and the outer wall of the vacuum flask, the heat transfer across the vacuum layer, the natural convection and radiation inside the flask and the phase change process of the PCMs. To realize the coupling of multiple thermal processes in the DTMS, the heat transfer equations based on equivalent thermal conductivity are constructed. In addition, the following reasonable assumptions are made:

(1) The vacuum layer is treated as a solid layer with extremely low thermal conductivity [18].
(2) Contact thermal resistance is ignored [28].
(3) The variations in material properties with temperature are neglected [40].
(4) The natural convection within the PCMs is neglected due to the high viscosity of the liquid phase in this system [27].

Based on the above assumptions, the operating process of the DTMS in high-temperature environment is simplified to a transient heat transfer process, which can be expressed as:

$$\rho c \frac{\partial T}{\partial t} = \nabla \cdot (k \nabla T) + Q \tag{1}$$

The average convective heat transfer coefficient between the outer surface of the vacuum flask and the high temperature downhole environment can be expressed as [25]:

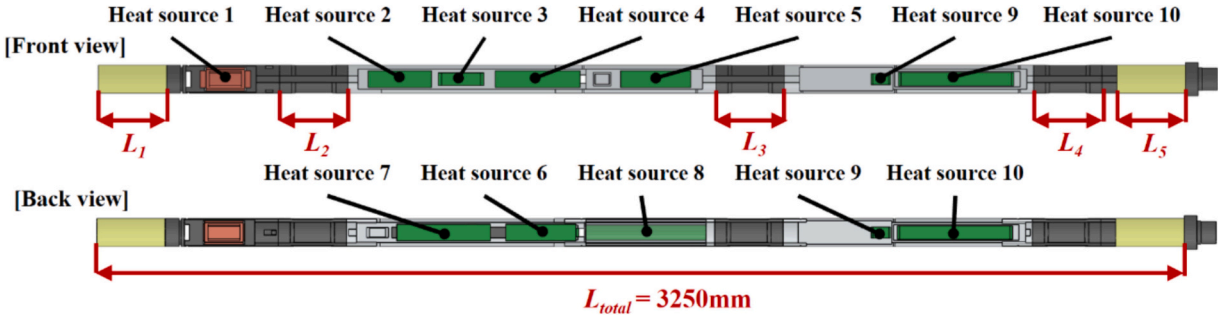

Fig. 2. Heat sources distribution and optimization design parameters.

$$h_L = \frac{1}{L}\int_0^L h(x)\mathrm{d}x = \frac{3k_{mud}}{4}\left[\frac{V}{45(r_h - r_t)^2\alpha_{mud}L}\right]^{\frac{1}{3}}\left[(11r_h - 5r_t)^{\frac{1}{3}} + \left(\frac{29r_h - 5r_t}{16}\right)^{\frac{1}{3}}\right] \quad (2)$$

An air gap exists between the inner wall of the vacuum flask at temperature T_f and the surface of the skeletons at temperature T_t, which induces natural convection and radiative heat transfer. The natural convective heat transfer Q_c within the annular air gap can be represented as [27]:

$$Q_c = \begin{cases} \dfrac{k_{\mathrm{air}}A(T_\mathrm{t} - T_\mathrm{f})}{R_\mathrm{t}\ln(R_\mathrm{f}/R_\mathrm{t})} & (Ra \le 6000) \\ \dfrac{0.13k_{\mathrm{air}}Ra^{0.25}A(T_\mathrm{t} - T_\mathrm{f})}{R_\mathrm{t}\ln(R_\mathrm{f}/R_\mathrm{t})} & (6000 < Ra \le 5\times10^4) \\ \dfrac{0.049k_{\mathrm{air}}Ra^{1/3}Pr^{0.074}A(T_\mathrm{t} - T_\mathrm{f})}{R_\mathrm{t}\ln(R_\mathrm{f}/R_\mathrm{t})} & (5\times10^4 < Ra < 7.17\times10^8) \end{cases} \quad (3)$$

The Rayleigh number Ra can be expressed as:

$$Ra = \frac{g\beta(T_\mathrm{t} - T_\mathrm{f})\delta^3}{\nu\alpha} \quad (4)$$

The coefficient of thermal expansion can be expressed as:

$$\beta = \frac{1}{T_{\mathrm{air}}} \quad (5)$$

For the radiative process, the heat transfer Q_r based on the Stefan-Boltzmann law can be expressed as:

$$Q_r = \frac{A\sigma(T_\mathrm{t}^4 - T_\mathrm{f}^4)}{\frac{1}{\varepsilon_\mathrm{t}} + \frac{R_\mathrm{t}}{R_\mathrm{f}}\left(\frac{1}{\varepsilon_\mathrm{f}} - 1\right)} \quad (6)$$

By combining multiple heat transfer processes of the air, the equivalent thermal conductivity of the annular air gap can be expressed as:

$$k_{eff} = k_{air} + \frac{Q_c + Q_r}{A(T_\mathrm{t} - T_\mathrm{f})} \quad (7)$$

The equivalent heat capacity method is adopted to simulate the phase change process of the PCM. The latent heat of the PCM is equated to a portion of the sensible heat capacity and a temperature transition range is defined for the phase change process. The governing equations can be expressed as [41]:

$$\rho_{pcm} = (1-\theta)\rho_{solid} + \theta\rho_{liquid} \quad (8)$$

$$c_{pcm} = \frac{1}{\rho_{pcm}}\left((1-\theta)\rho_{solid}c_{pcm,solid} + \theta\rho_l c_{pcm,liquid}\right) + L_{pcm}\frac{\partial M_{pcm}}{\partial T} \quad (9)$$

$$M_{pcm} = \frac{1}{2}\frac{\theta\rho_{liquid} - (1-\theta)\rho_{solid}}{\theta\rho_{liquid} + (1-\theta)\rho_{solid}} \quad (10)$$

Table 1
Material properties of each component [18,24,25].

Name	Material	Thermal conductivity ($W\cdot m^{-1}\cdot K^{-1}$)	Density ($kg\bullet m^{-3}$)	Heat capacity ($J\bullet kg^{-1}\bullet K^{-1}$)
Vacuum flask	Inconel 718	14.7	8240	436
Vacuum layer	Composite	0.0006	100	1200
Main control skeleton/ Motor driving skeleton	Aluminum alloy 7075	167	2710	896
Heat sources 2–10	Ceramic composites	16.5	2145	1136
Insulator shell	PEEK	0.25	2200	1000
Insulator core	Aluminum silicate wool	0.035	400	794.2
PCM container/ Terminal skeleton	Stainless steel	16.3	7930	500
PCM	LMPA	18.8	9580	146(s) 184(l)
Heat source 1/ Studs	Copper	400	8960	385

where θ is the temperature-dependent liquid fraction of the PCM. The phase transition is modeled as a smooth process. At the solidus temperature T_s and the liquidus temperature T_l, both the first and the second derivative of $\theta(T)$ are zero. The function can be expressed as:

$$\theta(T) = \begin{cases} 1 & T \ge T_l \\ \dfrac{1}{2} + \dfrac{15}{16}\cdot\dfrac{2T - (T_l + T_s)}{(T_l - T_s)} - \dfrac{5}{8}\cdot\left(\dfrac{2T - (T_l + T_s)}{(T_l - T_s)}\right)^3 + \dfrac{3}{16}\cdot\left(\dfrac{2T - (T_l + T_s)}{(T_l - T_s)}\right)^5 & T_s < T < T_l \\ 0 & T \le T_s \end{cases} \quad (11)$$

2.3. 3D numerical simulation setup and validation

The FEM was used to conduct 3D simulation of the heat transfer process. Based on the analysis in Section 2.2, the whole system was simulated as heat conduction problem. The thermal properties of the system materials were configured based on Table 1. The heat sinks incorporated LMPA as the encapsulated PCMs. The melting interval of the PCM was set as 72.7 °C–76.7 °C, with a latent heat of 37.2 kJ/kg [42]. An unstructured mesh was generated for the structure of the DTMS. The entire outer wall surface of the vacuum flask was set as a convective boundary condition, with an ambient temperature of 225 °C. The initial temperature of the instrument was set to 25 °C. The downhole electronic devices were considered as uniform volumetric heat sources and the heating power was set according to Table 2. The downhole operating process of the logging tool was simulated from 0 min to 1080 min, with a time step of 10 min.

Grid-independent validation was conducted to ensure the accuracy of simulation. Numerical models were computed with grid number of 4,338,032, 6,383,774, 7,431,438, 10,047,826, and 15,161,135, respectively. Fig. 3 shows the maximum temperature of the heat sources in DTMS with different grid number. Considering both the computational time and the accuracy, subsequent computations were performed using a meshing scheme comprising 7,431,438 elements. Moreover, the implemented 3D numerical heat transfer model has been rigorously validated through our previous studies [25,27,28,40]. Table 3

Table 2
Heating powers of different electronic devices.

Electronic device	Heating power (W)	Electronic device	Heating power (W)	Electronic device	Heating power (W)
Heat source 1	2.25	Heat source 5	1.75	Heat source 9	2.5
Heat source 2	1.25	Heat source 6	3.25		
Heat source 3	3.25	Heat source 7	1.25	Heat source 10	20.5
Heat source 4	1.25	Heat source 8	2.25		

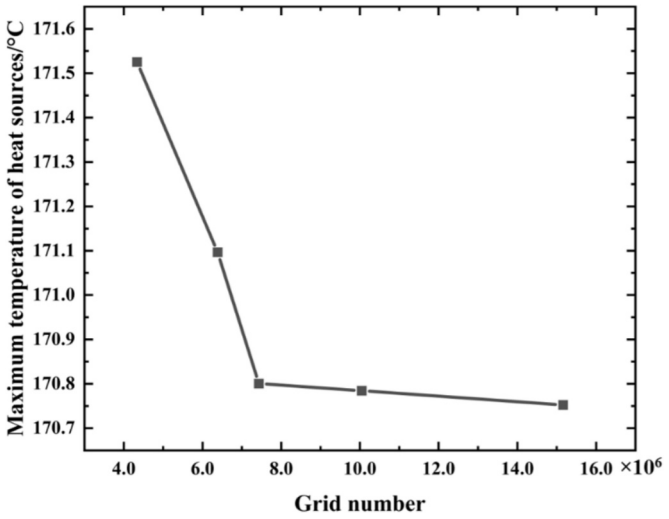

Fig. 3. Grid-independent analysis of 3D simulation.

Table 3
Validation of the numerical heat transfer model.

	Average temperature error (°C)	Maximum temperature error (°C)
Ref. [25]	/	Less than 5 °C
Ref. [27]	/	Less than 5 °C
Ref. [28]	3.02 °C	5.40 °C
Ref. [40]	1.60 °C	6.87 °C

summarizes the validation efforts by comparing experimental data with simulated results from these works, demonstrating the high accuracy of the numerical model.

To generate the high-fidelity dataset for machine learning training, the 3D simulations were executed using an automated batch processing script. This approach allowed for the efficient computation of thermal responses for the parameterized structural samples defined by the LHS method.

2.4. TRN establishment of DTMS

To enable rapid evaluation of thermal performance under different structural parameters, a TRN model of the system was established. Fig. 4 illustrates the node division strategy and the TRN of DTMS. The insulators, heat sinks and skeletons were divided into 11 main nodes along the axial direction of DTMS. Each node comprised components made of one or multiple materials. Taking the node "Main control skeleton 1" as an example, it integrated aluminum alloy skeleton, stainless steel shell and encapsulated PCM. These materials were treated as a unified node, whose equivalent thermal capacity was calculated by:

$$C_i = \sum_{j \in Node_i} \rho_j c_j V_j \tag{12}$$

Each heat source was modeled as an independent node and connected to the corresponding main node based on the spatial position in the skeleton. The heat conduction through copper studs between the heat sources and the skeletons was simulated by introducing thermal resistance between heat source nodes and skeleton nodes. The high-temperature environment was represented by a fixed-temperature boundary node. For the radial heat intrusion through the vacuum flask, radial thermal resistances (depicted as green elements in Fig. 4) were defined between main nodes and the environmental node. Axial heat transfer between adjacent main nodes was modeled using black axial thermal resistances. Notably, components in the thermal resistances network related to optimization variables were parameterized, enabling rapid evaluation of DTMS performance under different structural configurations.

For the computation of TRN, energy conservation is enforced at each node. For a given node i, the energy balance equation can be expressed as:

$$\sum_{j=1}^{m} \frac{T_j - T_i}{R_{ij}} + Q_i = C_i \frac{dT_i}{dt} \tag{13}$$

Based on Eq. (13), the TRN can be transformed into a system of linear differential equations for rapid solution.

For the axial plane thermal resistance between the neighboring main nodes, the calculation was performed by series and parallel relationship, which can be expressed as [26]:

$$R_{ij} = \frac{l_i}{2\sum_{m \in node_i} k_m S_m} + \frac{l_j}{2\sum_{n \in node_j} k_n S_n} \tag{14}$$

For the radial heat transfer through cylindrical walls, such as heat intrusion through the wall of the vacuum flask, the thermal resistance can be expressed as:

$$R_{i,radial} = \frac{\sum_{p=1}^{q} \left[\frac{1}{k_p} \ln\left(r_{p+1}/r_p\right) \right]}{2\pi l_i} \tag{15}$$

3. Optimization method

3.1. Transfer learning neural network (TLNN) model

The integration of physical principles into neural networks has emerged as a powerful approach to enhance model reliability and generalization. For instance, Di Natale et al. [43] successfully developed physically consistent neural networks for building thermal modeling by embedding physical laws into the network architecture. Inspired by such physics-guided methodologies, this study proposes a transfer learning neural network (TLNN) model that incorporates physical information into the modeling process.

Fig. 5 schematically illustrates the network topology and multi-stage training protocol. The training process of TLNN can be divided into 3 stages: 1) Pre-training using extensive TRN datasets to establish basic features of the network; 2) Freezing a subset of network parameters to preserve characteristic information; 3) Fine-tuning with high-fidelity 3D simulation datasets to enhance predictive accuracy. This strategy fundamentally differentiates the TLNN from ordinary neural networks, which typically update all parameters from a random initialization. By freezing the parameters of shallow layers, the TLNN effectively mitigates the risk of overfitting that compromises standard neural networks when trained on limited high-fidelity datasets.

The back propagation of the error is used to update the network parameter via gradient-based optimization, incorporating the learning rate concept. The updating algorithm can be formulated as:

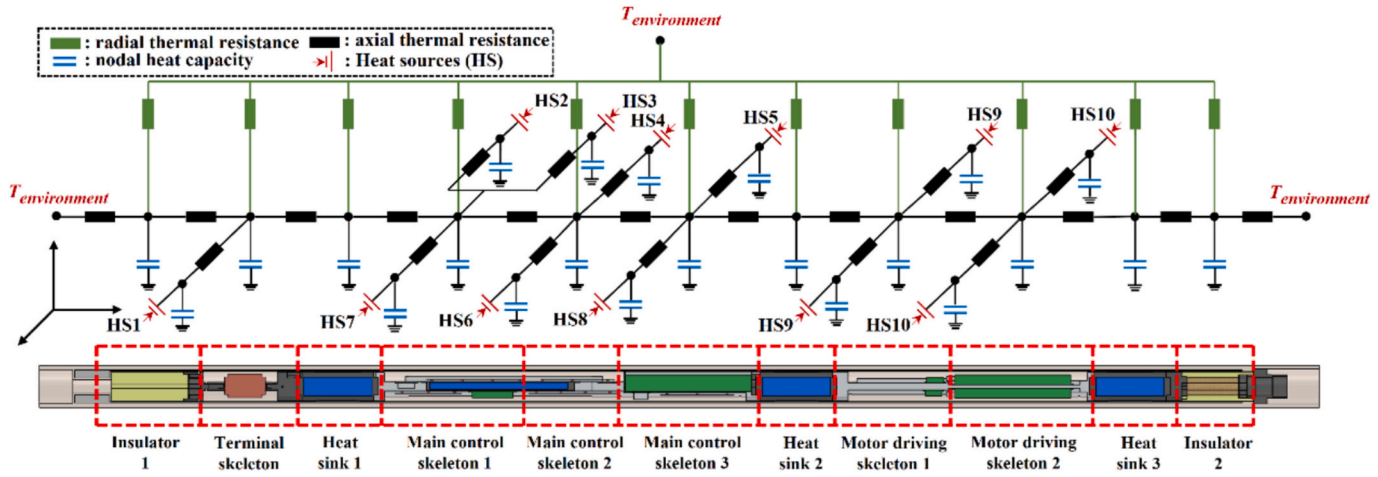

Fig. 4. The node division strategy and thermal network of the DTMS.

$$\psi_{(t+1)}^{[l]} = \psi_{(t)}^{[l]} - \eta(\psi^{[l]}) f\left(\frac{\partial \mathscr{L}}{\partial \psi_{(t)}^{[l]}}, \frac{\partial \mathscr{L}}{\partial \psi_{(t-1)}^{[l]}}\right) \tag{16}$$

To freeze specific network parameters during training, the learning rates η corresponding to these parameters are explicitly set to zero.

The TLNN employs 5 geometric structural parameters (L_1–L_5) as inputs and 10 heat source temperatures (T_1–T_{10}) as outputs. The network comprises 2 hidden layers with 10 and 20 neurons, respectively. The sigmoid activation function is implemented in the hidden layers, with a linear activation function adopted for the output layer. This architecture and training strategy are designed to balance model complexity with data constraints. A compact dual-hidden-layer structure was selected to mitigate overfitting during the fine-tuning phase, which relies on a limited dataset of 30 high-fidelity samples. Preliminary trials confirmed that a scale of approximately 30 neurons ensures robustness while preventing the network from memorizing specific data noise.

Specifically, the neuronal arrangement was empirically determined based on dimensional limits. The first layer (10 neurons) is set slightly larger than the input dimension, allowing for efficient extraction of the generalized physical laws from TRN data without feature redundancy. The second layer (20 neurons) is chosen to approach the upper bound imposed by the high-fidelity sample size. This configuration maximizes the network's ability to learn the complex fidelity gap without exceeding the capacity limit where overfitting becomes unmanageable.

Furthermore, the parameter freezing strategy ensures physical consistency. By freezing the weights ($w^{[1]}$, $w^{[2]}$) and biases ($b^{[1]}$) of the first hidden layer during fine-tuning, the physical laws governed by energy conservation are preserved. Only the remaining parameters ($b^{[2]}$, $w^{[3]}$, $b^{[3]}$) associated with the second hidden and output layers are updated, performing a terminal calibration. This ensures the model adapts to high-precision 3D data while maintaining the fundamental physical trends established during pre-training.

3.2. Optimization algorithm and designing process

Fig. 6 presents the workflow integrating the TLNN-based surrogate model with GA optimization. Initially, the LHS method was employed to randomly generate sufficient TRN samples and sparse 3D simulation samples within constrained parameter domains. Notably, the sampling processes for these two datasets were mutually independent to ensure distributional consistency. The maximum temperature of the heat sources serves as the objective function input for the optimization

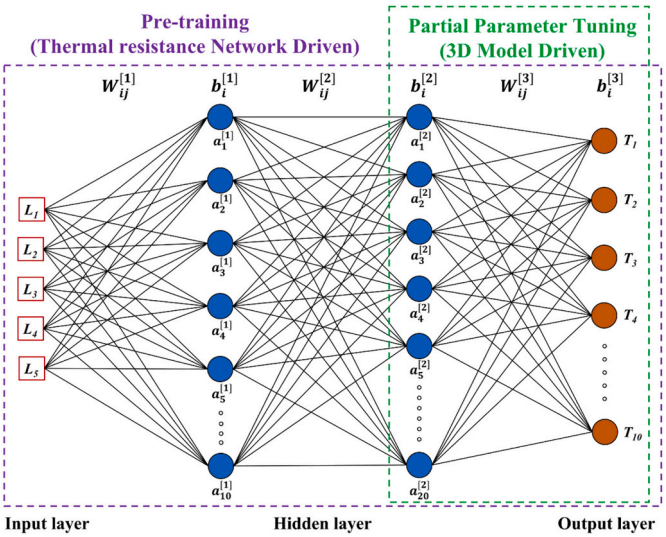

Fig. 5. Architecture and training protocol of TLNN.

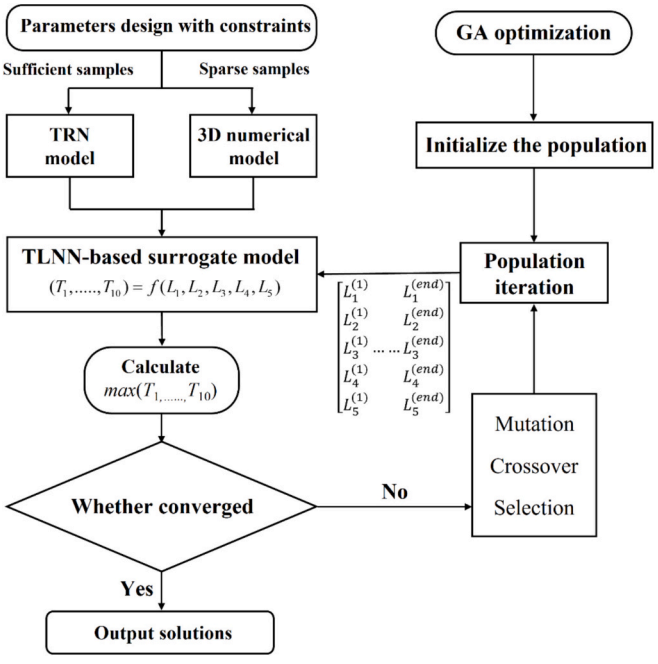

Fig. 6. Optimization process of DTMS based on surrogate model.

algorithm.

The GA was selected to govern the parameter optimization of the DTMS, diverging from the NM algorithm employed in previous studies. GA has demonstrated superior global search capabilities through biologically inspired operations—selection, crossover, and mutation—that drive population evolution toward optimal solutions. Coupled with the proposed surrogate model, the computational cost of the GA optimization is further reduced to achieve an efficient optimal design.

The optimization variables can be expressed as:

$$\text{Find} \quad [L_1, L_2, L_3, L_4, L_5] \tag{17}$$

The optimization objective is to minimize the operating temperature of the downhole electronic devices, which can be expressed as:

$$\text{Minimize} \quad \max(T_1, \ldots\ldots, T_{10}) \tag{18}$$

The total length of the five optimization variables is kept consistent, with each individual length of the variable bounded within specific ranges to satisfy manufacturing and assembly requirements. The constraints are defined as:

$$\text{Constraint} \quad \begin{cases} \sum_{i=1}^{5} L_i = 1022.5 \text{ mm} \\ 80 \text{ mm} \le L_i \le 450 \text{ mm} \end{cases} \tag{19}$$

The population size of the GA is configured to 150, the elite preservation ratio is 0.05, and the crossover probability is 0.8. The adaptive step mutation is implemented to ensure offspring solutions remain within the feasible design domain. To illustrate the necessity of GA in the optimization process, a comparative analysis is conducted in the following sections between the NM algorithm and GA.

4. Results and discussions

4.1. Accuracy analysis of TRN

The temperature results of the TRN model and 3D numerical model were first calculated under uniform structural parameters. Fig. 7(a) compares the simulated temperatures of 10 heat sources under identical structure. While the TRN model captures the general thermal response trends, quantitative discrepancies are evident when compared to the accurate 3D simulation results. The maximum temperature deviation between the two models is observed at Heat source 6, with the average error reaching 12.14 °C throughout the operation. The mean error across all heat sources is found to be 3.71 °C. Fig. 7(b) compares the averaged temperature results at different skeleton nodes. The results reveal that the maximum node temperature error is 7.39 °C and the average error is 5.36 °C. These considerable errors underscore that although the TRN model can offer a rapid, qualitative assessment of thermal performance, its standalone accuracy is insufficient for high-precision thermal optimization.

The maximum temperature error of the skeleton nodes exhibits smaller deviations than the maximum error of heat sources. This finding suggests that the source of error for both models is predominantly in the processing of model details. Specifically, heat transfer between skeletal nodes shows low sensitivity to geometric details, enabling TRN to approximate 3D results effectively. Conversely, heat sources are characterized by self-heating and confined heat dissipation pathways to the skeletons, making them more susceptible to geometric abstraction errors introduced by nodal simplification. These errors are justifiable given the fundamental discrepancies between computational dimensionality (TRN's 1D vs 3D model's spatial resolution) and resource demands.

4.2. Accuracy of TLNN-based surrogate model

Fig. 8 evaluates the predictive accuracy of the TLNN trained with varying numbers of 3D numerical samples. To ensure a rigorous and fair comparison, a strict data splitting protocol was implemented using LHS. Specifically, 400 low-fidelity TRN samples were generated for pre-training. For quantitative validation, an independent testing set comprising 20 high-fidelity samples was generated. Crucially, this testing set was mutually exclusive from any training subsets used in the subsequent analysis. These testing samples were strictly isolated from the training process to prevent data leakage. All surrogate models were evaluated on this identical testing set to validate their generalization capabilities on unseen data. The predictive effect of the surrogate model is evaluated by RMSE and R^2, which can be expressed as:

$$RMSE = \left(\sum_{i=1}^{n} [y_i - \hat{y}_i]^2 / n \right)^{1/2} \tag{20}$$

$$R^2 = 1 - \sum_{i=1}^{n} (y_i - \hat{y}_i)^2 / \sum_{i=1}^{n} (y_i - \bar{y})^2 \tag{21}$$

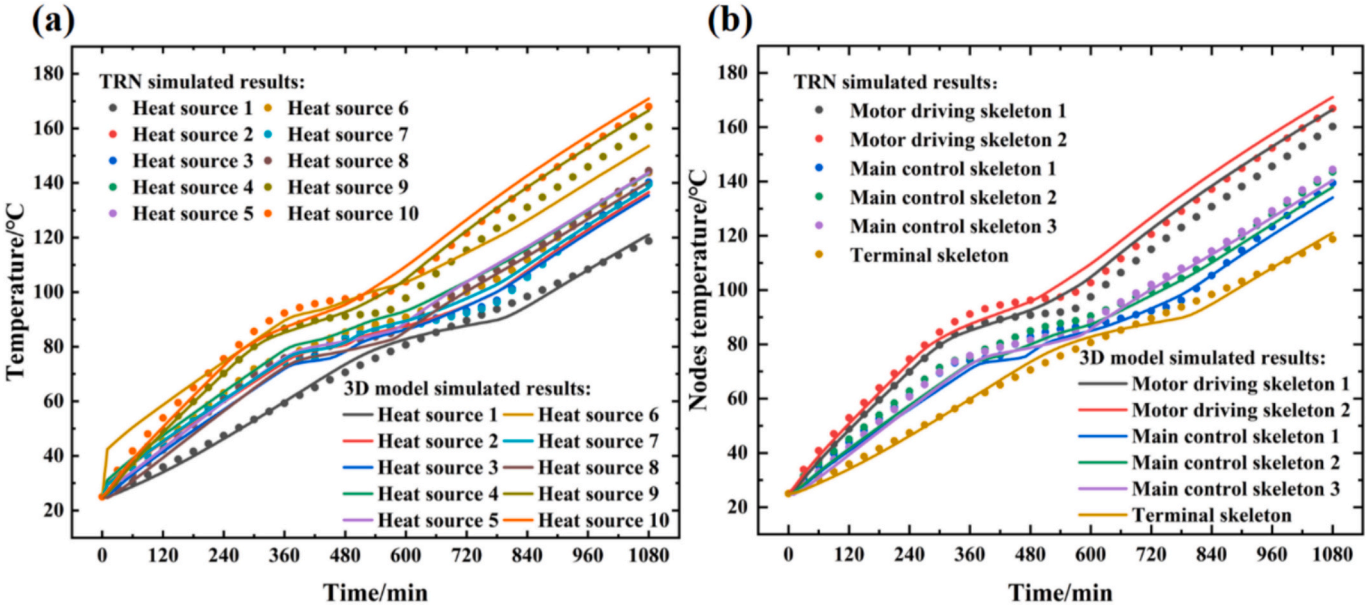

Fig. 7. The comparative results between TRN and 3D numerical model: (a) temperature of ten heat sources, (b) averaged temperature of different skeleton nodes.

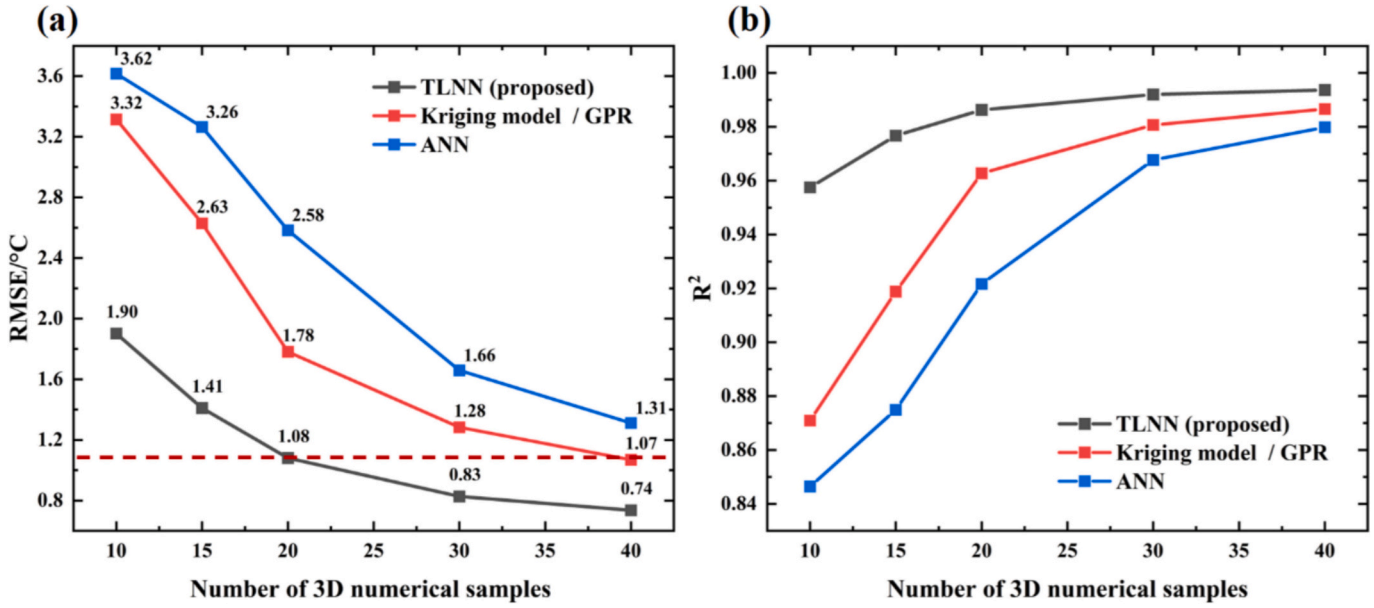

Fig. 8. Prediction effect of TLNN under training of different 3D numerical samples: (a) RMSE, (b) R^2.

Fig. 8(a) compares the RMSE of maximum heat source temperature predictions between TLNN, Kriging model, and ANN surrogate models under identical training sample sizes. It can be seen that the TLNN demonstrates superior accuracy, particularly under data scarcity conditions. The TLNN model, with only 20 high-fidelity samples, can achieve the same accuracy comparable to that attained by the Kriging and ANN models requiring as many as 40 samples. This capability effectively reduces the number of computationally expensive 3D simulations required for surrogate model construction by at least 50% to achieve a similar degree of accuracy, thereby significantly shortening the model development time. With 30 high-fidelity samples, it achieves 35.16% and 50% lower RMSE than Kriging model and ANN, respectively. Notably, TLNN's RMSE falls below 1 °C at the sample size of 30, establishing it as the configuration for subsequent optimizations.

Fig. 8(b) reveals TLNN's exceptional generalization capability, attaining the R^2 of the maximum heat source temperature more than 0.99 on unseen test cases when trained with 30 3D samples. This performance surpasses both benchmark models, which is attributed to TLNN's two-stage learning strategy: 1) capturing global thermal patterns from cost-effective TRN data, 2) refining localized thermal results via

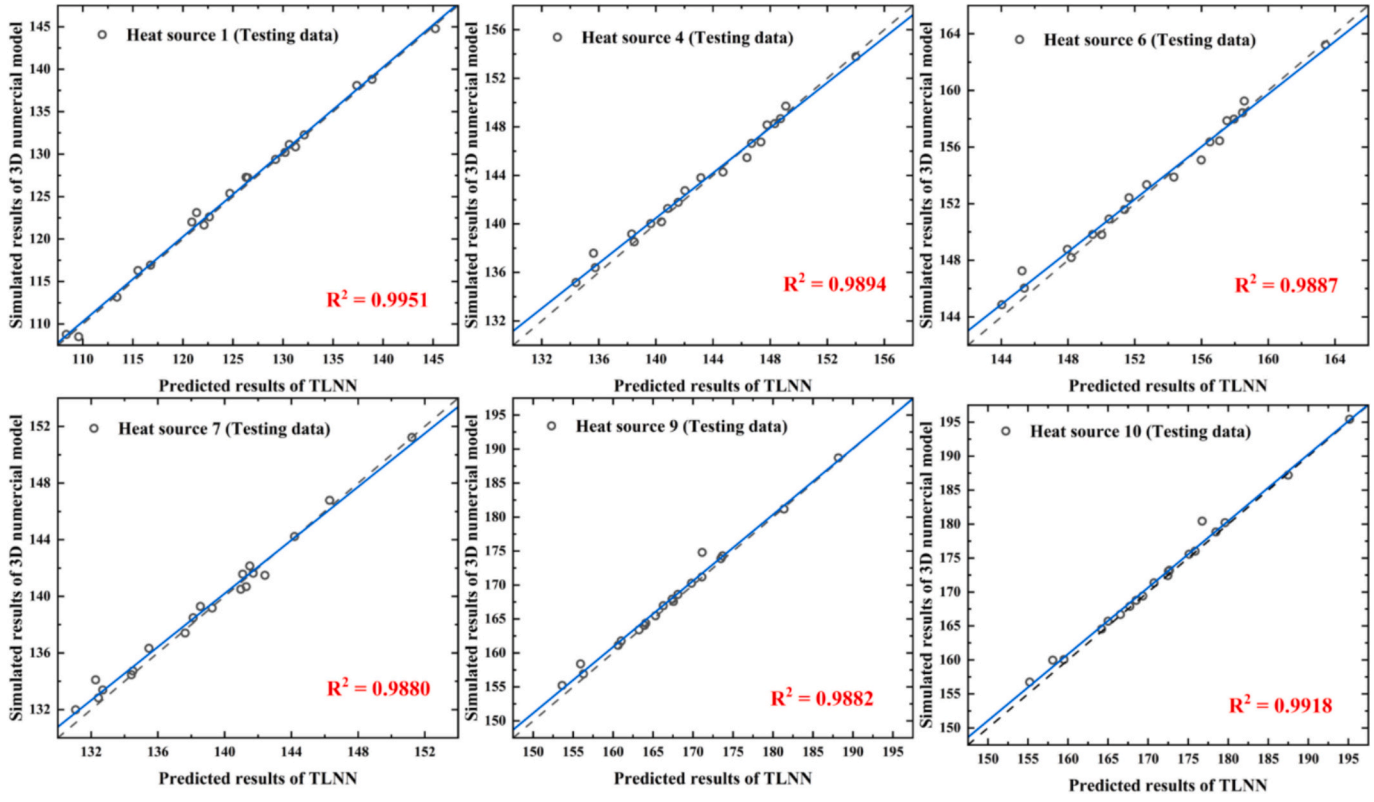

Fig. 9. R^2 performance of the surrogate model on partially selected heat sources.

selective 3D simulation fine-tuning. These results conclusively demonstrate the efficacy of hybrid TRN and 3D numerical simulation modeling in developing high-precision surrogate models with minimal computational cost.

Fig. 9 further demonstrates the predictive capability of the TLNN-based surrogate model, trained with 30 3D numerical samples, for the temperatures of key heat sources within the DTMS. On the test set of 20 independent cases, the predicted and simulated results exhibit correlation coefficients exceeding 0.988, validating the capability of the surrogate model to reliably predict temperature distributions. Crucially, this strong predictive performance for individual heat sources, including those that may determine the system's peak temperature, ensures that the overall maximum temperature predictions derived from the surrogate model are also sufficiently precise, thereby confirming its viability for precise thermal optimization.

Furthermore, the proposed framework offers a critical advantage in computational efficiency through parallelization. Unlike sequential optimization strategies that require iterative model updates and serial execution of simulations, the sampling strategy employed in this study enables the simultaneous execution of all high-fidelity 3D simulations on computing clusters. This capability drastically shortens the design cycle, making it particularly suitable for engineering applications where parallel computing resources are available but individual simulation costs are high.

4.3. Analysis of the TLNN-GA optimization process

A comparative analysis of the NM algorithm and GA was conducted for optimizing the structure of DTMS. Fig. 10(a) tracks the NM optimization trajectories under four distinct initial parameter sets. The algorithm demonstrates significant performance variability depending on the initial conditions. As the black line shows, when initialized with a structure configuration yielding maximum temperature of 191.19 °C, 92 iterations were required yet achieved the temperature reduction of only 11.21 °C, stagnating at 179.98 °C. Although other initial parameter sets marginally enhanced convergence, all cases except the optimal set (initial parameters 4) failed to achieve satisfactory results. Moreover, the NM-FEM optimization scheme demanded over 79 iterations, exceeding the total 3D simulations required by the proposed TLNN-based surrogate model.

Fig. 10(b) compares structure design before and after optimization across initial parameter sets. Substantial discrepancies emerged due to local optima traps: Initial parameters 1 (poor initial performance) showed minimal parameter adjustments, constrained by domain boundaries and gradient misalignment. In contrast, the optimization results for initial parameter 4 differ significantly in structural parameters from those of initial parameter 1. The value of L_2/L_4 after optimization with initial parameters 4 is 0.26, while the value with initial parameters 1 is 4.41, showing a 17-fold difference. These findings conclusively demonstrate NM's critical dependence on initial parameters and suboptimal search efficiency for distributed DTMS optimization, necessitating advanced metaheuristic approaches for robust and efficient design exploration.

Fig. 11(a) delineates the GA optimization process for the DTMS. Configured with a population size of 150 individuals, the GA converges after 1111 generations. Leveraging the surrogate model for fitness evaluations, the entire optimization completes within minutes. During iterations, the mean fitness of the population initially decreases rapidly before gradually converging alongside the best fitness. The maximum temperature of the heat sources reduces from 159.17 °C to 154.52 °C in this process, yielding the optimal structural configuration. Fig. 11(b) compares structural parameters (L_1-L_5) between the best individuals in the initial and final generations. The values of structural parameters L_1, L_2, L_3, L_4, and L_5 are 142.99 mm, 160.54 mm, 151.27 mm, 362.01 mm and 205.70 mm at the first generation of the population, respectively, while the best individuals obtained at the last generation are 80.03 mm, 80.07 mm, 275.98 mm, 366.39 mm, and 220.02 mm. The structural parameter distribution of the DTMS exhibits small variation, reflecting the strategic search behavior of the GA. The observation indicates that the initial population sampling of GA effectively narrows the design space, enabling convergence through iterative refinements rather than radical parametric redesigns. The mutation operations further enhance the global search capability by maintaining genetic diversity.

The optimized structure was further validated through 3D numerical simulations and compared with the surrogate model predictions. Fig. 12 presents the comparison results. The maximum temperature error across the 10 heat sources is 0.81 °C, with an average error of 0.61 °C, demonstrating the high accuracy of the surrogate model. These findings indicate that the optimization results obtained by the TLNN-based surrogate model meet the precision requirements for DTMS design.

Notably, the most time-consuming step of surrogate-based optimization for DTMS lies in generating 3D numerical simulation samples. Only 30 high-fidelity samples are required to construct an accurate surrogate model for the proposed TLNN framework, reducing computational resource consumption by 62% compared to the NM-FEM optimization. This approach eliminates the need for manual selection of

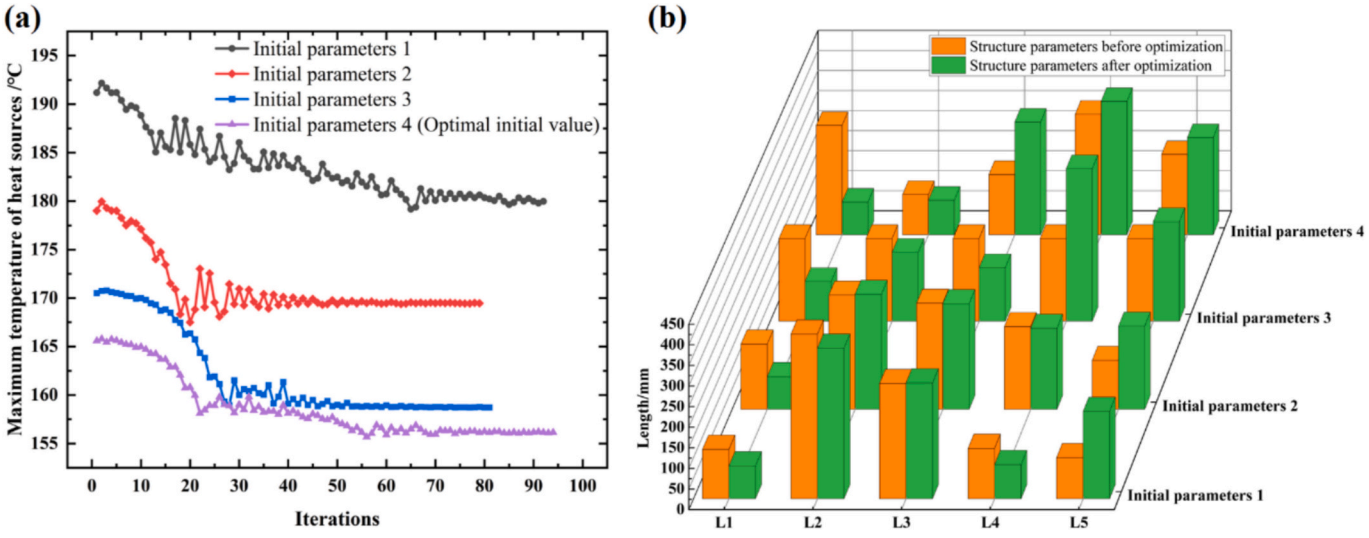

Fig. 10. Optimization process of NM algorithm with different initial parameters: (a) temperature versus iterations, (b) structure parameters before and after optimization.

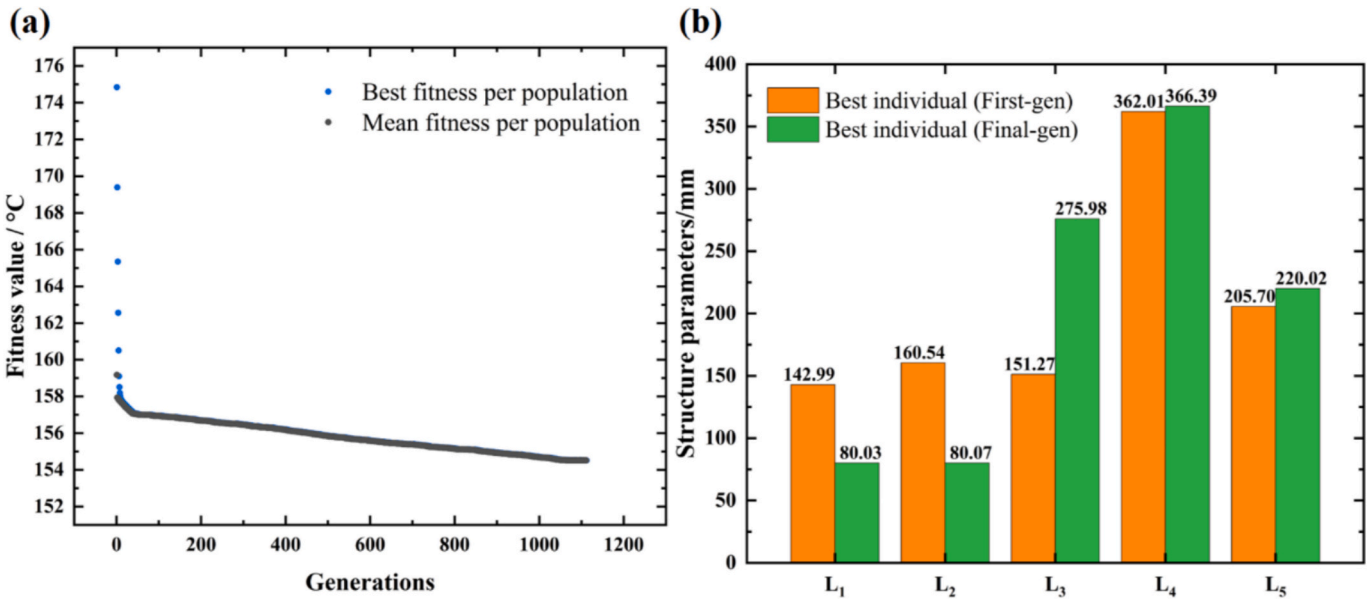

Fig. 11. Optimization process of GA: (a) fitness value versus iterations, (b) structure parameters before and after optimization.

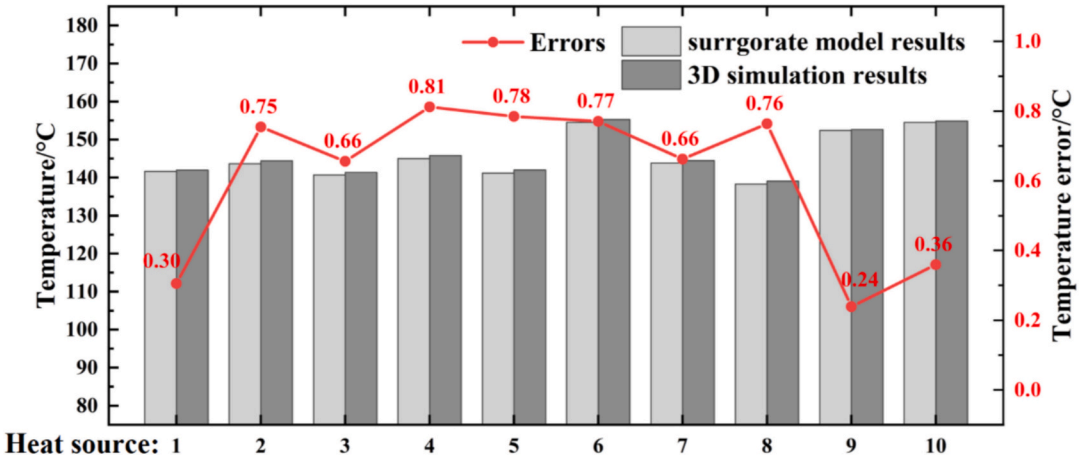

Fig. 12. Comparison of heat source temperatures between surrogate model and 3D simulation.

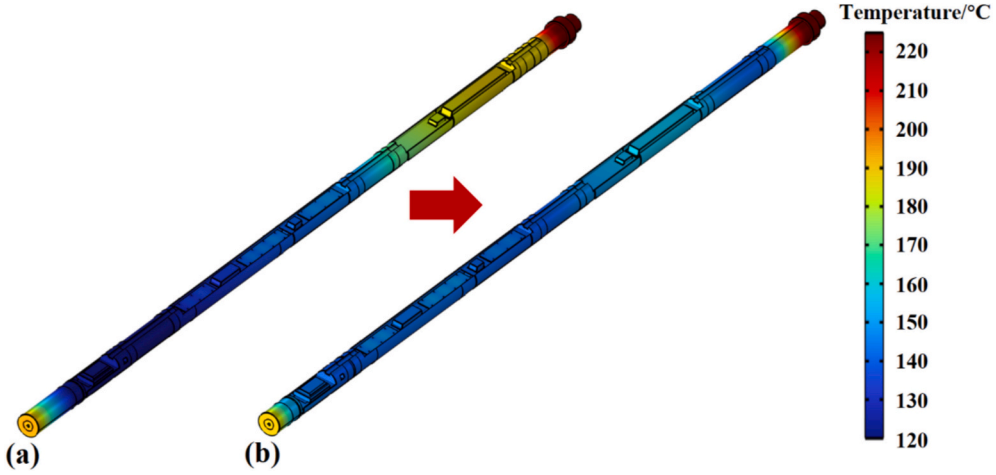

Fig. 13. Temperature field of the DTMS at the final moment of operation: (a) before optimization, (b) after optimization.

initial parameters and avoids resource-intensive trial-and-error iterations, establishing an effective pathway for the optimization of DTMS.

4.4. Thermal performance after optimization

Fig. 13 shows the temperature field of the DTMS at the final moment of operation before and after optimization. Before optimization, the mismatch between the heat sink length distribution and the heat source power distribution results in significantly higher temperatures in the motor driving skeleton compared to other parts of the system, while the main control skeleton exhibits a low-temperature state. This leads to a substantial temperature difference within the system, which is detrimental to controlling the temperature of electronic devices. Additionally, the larger heat exchange area of insulator 2 with the high-temperature environment, combined with its shorter length, causes a mismatch between thermal insulation performance and heat intrusion, resulting in excessively high temperatures at heat source 10. In contrast, the optimized system exhibits excellent temperature uniformity, fully utilizing the heat storage capacity of the system. The relative lengths of insulator 1 and 2 are also adjusted based on their structural characteristics, demonstrating superior thermal insulation performance.

Fig. 14 shows the temperature curves versus time of the heat sources in DTMS. Before optimization, the highest temperature at heat source 10 reached 187.88 °C, while the temperature at heat source 1 was only 108.51 °C, resulting in a temperature difference of 79.37 °C across the system. After optimization, the temperature difference among electronic devices is reduced to 16.22 °C, achieving greater temperature uniformity. The results indicate that after operating for 1080 min in a 225 °C environment, the maximum heat source temperature of the optimized system was 155.29 °C, a reduction of 32.59 °C compared to the pre-optimization system, meeting the thermal requirements for downhole operations.

Fig. 15(a) compares the thermal accumulation of various skeletons and heat sinks in the system before and after optimization. The thermal accumulation of the main control skeleton remains almost unchanged after optimization, reaching 1019.5 kJ at the final moment. The motor driving skeleton exhibits a significant reduction in thermal accumulation after 360 min of operation, which is attributed to structural modifications in insulator 2 and heat sink 3 that mitigate heat concentration near high-power electronic devices. Correspondingly, the optimization process reduces the lengths of insulator 1 and heat sink 1, leading to increased thermal accumulation in rear skeleton. Since the rear skeleton was at a lower temperature before optimization, the increased thermal accumulation after optimization contributes to improved temperature uniformity. Additionally, the total thermal accumulation of the heat sinks rises from 1733.22 kJ to 1833.19 kJ, showing an increase of 5.76%.

Fig. 15(b) and (c) compare the thermal accumulation in individual heat sinks and all skeletons at the final moment before and after optimization. The total thermal accumulation of the heat sinks shows minimal change. However, the thermal accumulation of individual heat sinks varies significantly. Specifically, the proportion of thermal accumulation in heat sink 3 increases from 10.15% to 22.87%, consistent with its proximity to the high-power heat source 10. Conversely, the thermal accumulation proportion of heat sink 1 decreases from 16.56% to 5.45%, facilitating local heat storage near the heat sources and reducing excessive temperature gradients within the system due to long heat transfer paths.

Fig. 16 compares the heat transferred along different directions in the main control skeleton and motor driving skeleton of DTMS before and after optimization. The blue bars represent the total heat generated by all heat sources on each skeleton. For example, the heat sources in main control skeleton generate 1490 kJ (23 W × 1080 min). The orange and green bars indicate the heat flow through the left and right cross-sections, respectively, which can be calculated by:

$$Q_{flux} = \int_0^t \iint_{S_{axial}} q_{flux} dA dt \tag{22}$$

Fig. 16(a) illustrates the heat transfer directions in DTMS before optimization. The majority of heat in the motor driving skeleton flows leftward to heat sink 2 (668.80 kJ), with only 113.75 kJ flowing rightward to heat sink 3. This indicates that heat sink 3 fails to effectively store heat due to the suboptimal length distribution of insulator 2 and heat sink 3. Similarly, due to the excessive length of heat sink 1, heat from the main control skeleton predominantly flows to the left side. Fig. 16(b) depicts the heat transfer directions after optimization. By increasing the length of heat sink 3, the motor driving skeleton gains an additional rightward heat transfer path to heat sink 3, reducing heat accumulation. Bidirectional heat dissipation significantly reduces the temperature gradient in a single direction, enhancing the performance of DTMS. Additionally, reducing the length of the heat sink adjacent to

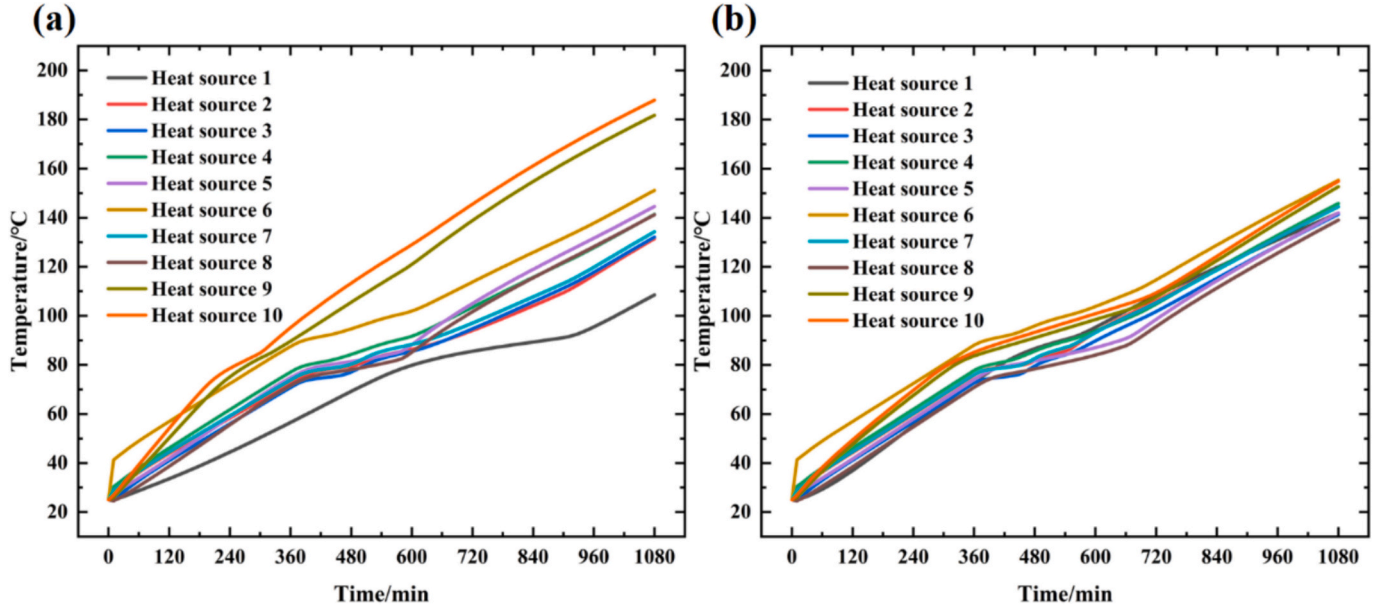

Fig. 14. Temperature curves versus time of the heat sources in DTMS: (a) before optimization, (b) after optimization.

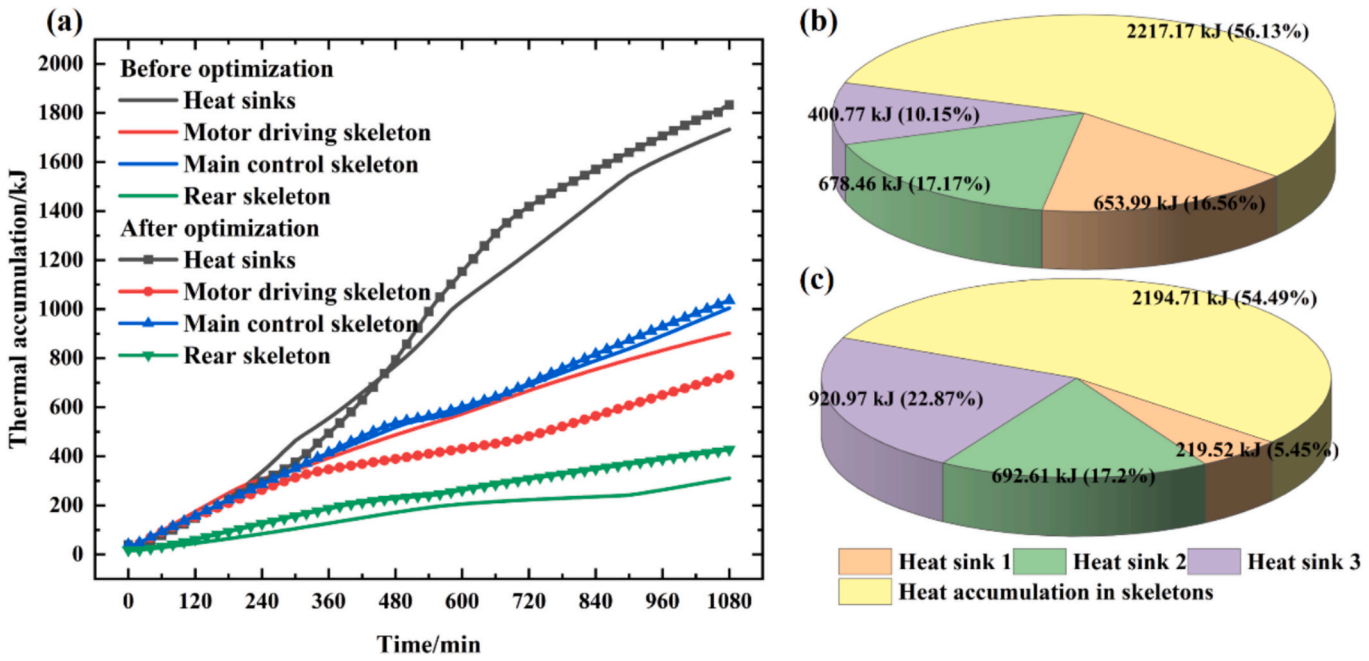

Fig. 15. Thermal accumulation analyses: (a) various skeletons versus time (b) various heat sinks at the final moment.

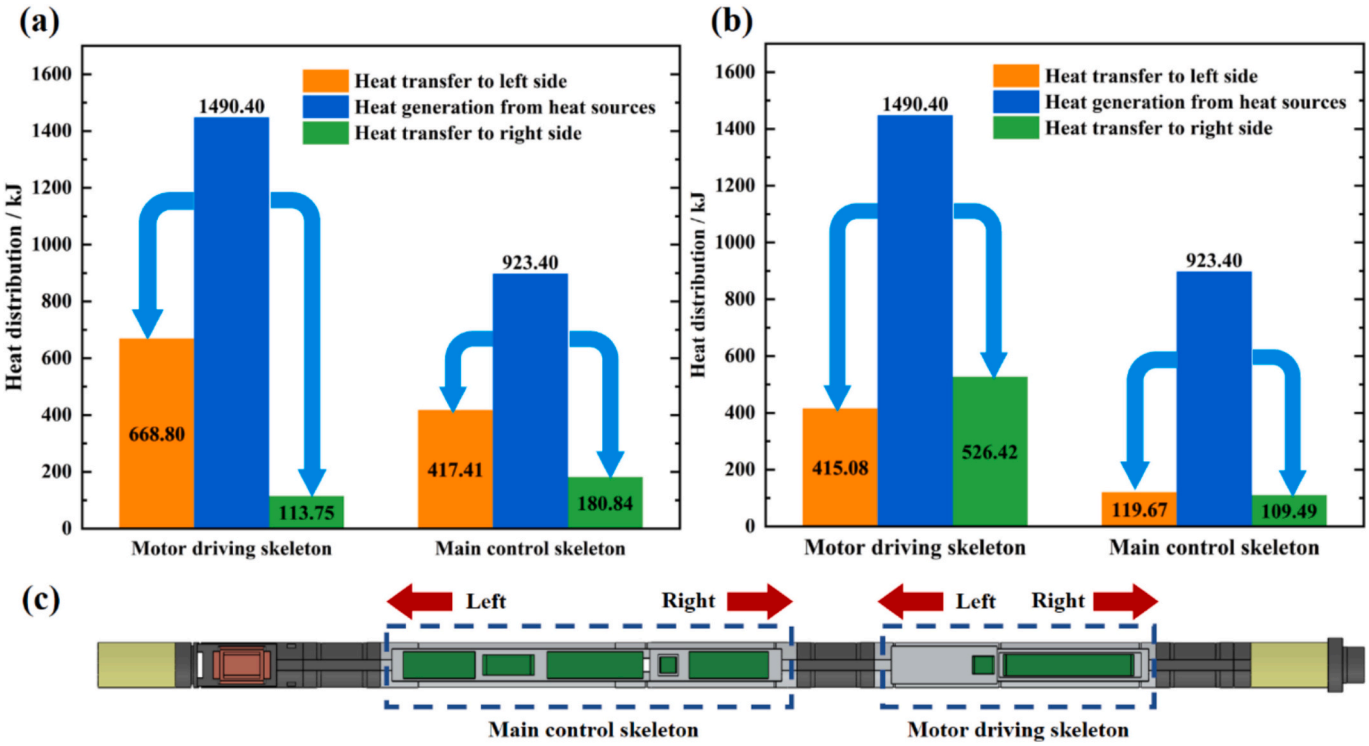

Fig. 16. Heat transferred along different directions in the two main skeletons: (a) before optimization, (b) after optimization, (c) direction identification.

the main control skeleton allows more heat to remain, promoting the temperature uniformity within DTMS.

4.5. Impact of operational conditions on optimal design

Fig. 17(a) shows the optimal structural parameters of the DTMS under various ambient temperature conditions. Four typical downhole environments (150 °C, 175 °C, 205 °C, and 225 °C) are selected for analysis. As ambient temperature increases, the length of insulator 2 increases from 168.56 mm to 220.02 mm. Correspondingly, the length of heat sink 2 decreases from 322.92 mm to 275.98 mm. This can be attributed to the more severe effect of heat intrusion at higher ambient temperatures, necessitating a reduction in the length of heat sink 2 to allow for an extended insulator 2. On average, for every 25 °C increase in ambient temperature, the length of insulator 2 increases by 7.8%, while the length of heat sink 2 decreases by 4.8%. The rest of the structure remains almost unchanged, indicating that the optimal main structure of the DTMS does not undergo significant changes with

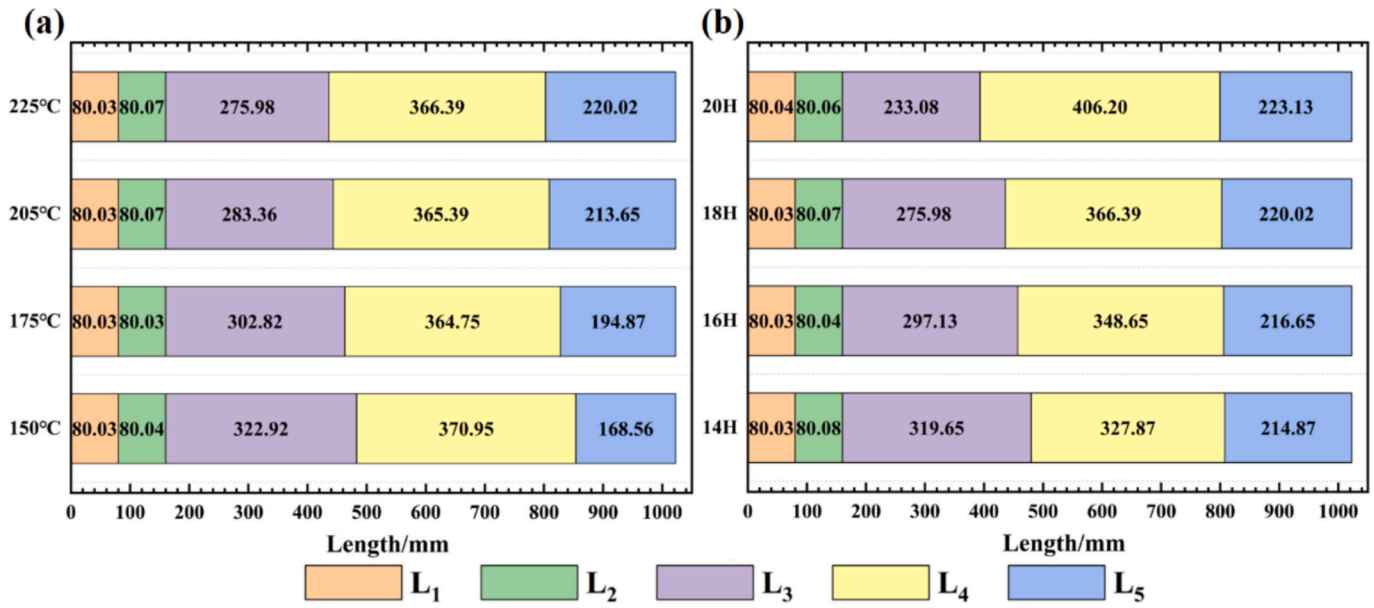

Fig. 17. Optimal structure under different operating conditions: (a) different downhole environment temperature, (b) different operating times.

variations in ambient temperature.

Fig. 17(b) presents the optimal structural parameters under different operating times. Typical operating times of 14 h, 16 h, 18 h, and 20 h are analyzed. The results show that as the operating time increases, the length of heat sink 3 increases from 327.87 mm to 406.20 mm, while the length of heat sink 2 decreases from 319.65 mm to 233.08 mm. This suggests that the impact of high-power heat sources and ambient heat intrusion becomes increasingly significant over time. On average, for each additional hour of operation, the length of heat sink 3 increases by 3.2%, while the length of heat sink 2 decreases by 4.5%. The rest of the structural parameters remain nearly unchanged, demonstrating the robustness of the structural layout under varying external boundary conditions. Therefore, the optimized design maintains topological consistency, allowing it to be effectively applied to a range of typical downhole environments with only minor dimensional adjustments.

5. Conclusions

This study proposes an efficient TLNN optimization framework based on surrogate modeling for optimizing the structure of DTMS. The main conclusions are summarized as follows:

1) The proposed TLNN-based surrogate model was demonstrated to effectively integrate the computational efficiency of the TRN and the accuracy of 3D simulations. Compared with conventional Kriging and ANN models, the TLNN model achieved 35.16% and 50% lower RMSE respectively with an equivalent training sample size, while also halving the high-fidelity sample requirement for achieving a comparable model accuracy.
2) When integrated with a Genetic Algorithm (GA), the TLNN-surrogate-driven optimization framework effectively searched design spaces to identify high-quality solutions and avoid local entrapment. Compared with the NM-FEM optimization framework, the proposed method avoided local optima and manual parameter initialization, while reducing computational cost by 62%.
3) Application of this framework to the DTMS resulted in a significant enhancement of thermal performance: the maximum temperature of the heat sources was reduced by 32.6 °C, the internal temperature difference dropped by 63.15 °C, and the heat source temperature remained below 160 °C after 18 h of operation.
4) The optimized structure demonstrated robust performance across a range of environment temperatures and operating times. Although slight adjustments were required for specific components, the fundamental layout proved highly effective under varying conditions.

Overall, this study offers an efficient and powerful optimization framework for the advanced design of complex thermal energy storage systems. Massive pre-training datasets can be generated by TRN to cover the expanded design space, minimizing reliance on expensive high-fidelity samples since fine-tuning targets only the residual fidelity gap. The proposed methodology can be adapted to other thermodynamic conditions or geometries by replacing the low-fidelity physical model, making it a valuable and transferable tool for optimizing other thermal systems.

CRediT authorship contribution statement

Siqi Zhang: Writing – original draft, Methodology, Conceptualization. **Chao Deng:** Validation, Investigation, Data curation. **Fulong Wei:** Validation, Data curation. **Jiacheng Li:** Validation, Formal analysis. **Xiaobing Luo:** Writing – review & editing, Supervision, Funding acquisition. **Jinlong Ma:** Writing – review & editing, Funding acquisition.

Declaration of competing interest

The authors declare that they have no known competing financial interests or personal relationships that could have appeared to influence the work reported in this paper.

Acknowledgements

This research was supported by National Key Research and Development Program of China (2022YFC2204400) and the Open Fund of Science and Technology on Thermal Energy and Power Laboratory (No. TPL 2022B02).

Data availability

Data will be made available on request.

References

[1] Mingming Jiang, Quanyou Liu, Geochemical characteristics of ultra-deep natural gases, Org. Geochem. 203 (2025) 104964.
[2] Zicheng Cao, Anlai Ma, Xu Qinqi, Quanyong Pan, Kai Shang, Fan Feng, Yongli Liu, Geochemical characteristics and exploration significance of ultra-deep Sinian oil and gas from Well Tashen 5, Tarim Basin, NW China, Energy Geosci. 5 (1) (2024) 100217.
[3] Zhixin Wen, Jianjun Wang, Zhaoming Wang, Zhengjun He, Chengpeng Song, Xiaobing Liu, Ningning Zhang, Tianyu Ji, Analysis of the world deepwater oil and gas exploration situation, Pet. Explor. Dev. 50 (5) (2023) 1060–1076.
[4] He Dengfa, Jia Chengzao, Zhao Wenzhi, Xu Fengyin, Luo Xiaorong, Liu Wenhui, Tang Yong, Gao Shanlin, Xiujuan Zheng, Li Di, Research progress and key issues of ultra-deep oil and gas exploration in China, Pet. Explor. Dev. 50 (6) (2023) 1333–1344.
[5] Mike Hanson, Lee Hyson, Hamish Munro, Guy Wheater, Wireline cable dynamics & wellbore diagnostics in the deepwater logging environment, in: SPWLA Annual Logging Symposium SPWLA, 2024 p. D051S025R002.
[6] Christian Zeeden, Arne Ulfers, Simona Pierdominici, Mehrdadsardar Abadi, Mathias Vinnepand, Thomas Grelle, Katja Hesse, Katharina Leu, Thomas Wonik, Downhole logging data for time series analysis and cyclostratigraphy, Earth Sci. Rev. 241 (2023) 104436.
[7] Amal Habeeb, Introduction and investigation into oil well logging operations, J. Eng. NY 29 (02) (2023) 72–91.
[8] Hengrui Zhang, Su Yinao, Maolin Liao, Zhiqiang Zhu, Haiyan Zhang, Zhi Li, Junyi Chang, Wu Hongyu, Ke Liu, Thermal management of drilling fluids with phase change materials in ultra-high temperature wells, Appl. Therm. Eng. 274 (2025) 126601.
[9] Yota Suzuki, Takashi Akatsuka, Yusuke Yamaya, Norihiro Watanabe, Kyosuke Okamoto, Kazumi Osato, Tatsuya Kajiwara, Yasuo Ogawa, Toru Mogi, Noriyoshi Tsuchiya, Estimation of an ultra-high-temperature geothermal reservoir model in the Kakkonda geothermal field, northeastern Japan, Geothermics 105 (2022) 102525.
[10] Hongwei Yang, Jun Li, Hui Zhang, Jiwei Jiang, Boyun Guo, Reyu Gao, Geng Zhang, Thermal behavior prediction and adaptation analysis of a reelwell drilling method for closed-loop geothermal system, Appl. Energy 320 (2022) 119339.
[11] Jiale Peng, Jiacheng Li, Siqi Zhang, Guanying Xing, Jinlong Ma, Bofeng Shang, Xiaobing Luo, Experimental and numerical investigation on a hybrid high-temperature downhole thermal management system integrating liquid cooling and phase change material, Appl. Therm. Eng. 124804 (2024).
[12] Mohamedshafik Khaled, Ningyu Wang, Pradeepkumar Ashok, Dongmei Chen, Eric van Oort, Strategies for prevention of downhole tool failure caused by high bottomhole temperature in geothermal and high-pressure/high-temperature oil and gas wells, SPE Drill. Complet. 38 (02) (2023) 243–260.
[13] Dhirenk Pradhan, Davidc Moore, Amatt Francis, Jacob Kupernik, Wjoshua Kennedy, Nicholasr Glavin, Royh Olsson III, Deep Jariwala, Materials for high-temperature digital electronics, Nat. Rev. Mater. (2024) 1–18.
[14] Fei Li, Yuan Liu, Xueying Ma, Yuqi Tan, Design of 150° C DC–DC converter based on Flyback topology for downhole drilling equipment, IEEE Access 11 (2023) 111126–111132.
[15] Mohamedshafik Khaled, Ningyu Wang, Pradeepkumar Ashok, Eric van Oort, Downhole heat management for drilling shallow and ultra-deep high enthalpy geothermal wells, Geothermics 107 (2023) 102604.
[16] Jun Jing, Yixiang Huangfu, Xiaohua Zhu, Yu Jinhang, Yang Tian, Experimental investigation on heat transfer characteristics and thermal optimization methods of the storage-type downhole visual tool, Appl. Therm. Eng. 258 (2025) 124589.
[17] Jiale Peng, Chao Deng, Fulong Wei, Siqi Ding, Hu Run, Xiaobing Luo, A hybrid thermal management system combining liquid cooling and phase change material for downhole electronics, J. Energy Storage 72 (2023) 108610.
[18] Jiale Peng, Yujun Wang, Siqi Ding, Chao Deng, Fulong Wei, Xiaobing Luo, Rapid detection of the vacuum failure of logging tools based on the variation in equivalent thermal conductivity, Int. J. Therm. Sci. 188 (2023) 108245.
[19] Vc Midhun, S. Suresh, S.R. Akhilkrishnan, Effect of vacuum insulation panel integration in phase change material-based passive thermal management system for electronics package exposed to hot air environment, J. Energy Storage 53 (2022) 105180.
[20] Junjie He, Qiuwang Wang, Wu Jian, Yongmin Zhang, Wenxiao Chu, Hybrid thermal management strategy with PCM and insulation materials for pulsed-power source controller in extreme oil-well thermal environment, Appl. Therm. Eng. 214 (2022) 118864.
[21] Yupu Ma, Bofeng Shang, Run Hu, Xiaobing Luo, Thermal management of downhole electronics cooling in oil & gas well logging at high temperature, in: 2016 17th International Conference on Electronic Packaging Technology (ICEPT), IEEE, 2016, pp. 623–627.
[22] Jiale Peng, Wei Lan, Yujun Wang, Yiming Ma, Xiaobing Luo, Thermal management of the high-power electronics in high temperature downhole environment, in: 2020 IEEE 22nd Electronics Packaging Technology Conference (EPTC), IEEE, 2020, pp. 369–375.
[23] Bofeng Shang, Yupu Ma, Hu Run, Chao Yuan, Hu Jinyan, Xiaobing Luo, Passive thermal management system for downhole electronics in harsh thermal environments, Appl. Therm. Eng. 118 (2017) 593–599.
[24] Wei Lan, Jiawei Zhang, Jiale Peng, Yiming Ma, Shuling Zhou, Xiaobing Luo, Distributed thermal management system for downhole electronics at high temperature, Appl. Therm. Eng. 180 (2020) 115853.
[25] Jiale Peng, Zhibin Tian, Chao Deng, Fulong Wei, Bofeng Shang, Xiaobing Luo, Durable and reliable thermal management system with superior temperature uniformity for sidewall coring tool in extreme thermal environments, Therm. Sci. Eng. Prog. 51 (2024) 102635.
[26] Fulong Wei, Wei Lan, Chao Deng, Jiale Peng, Xiaobing Luo, A transient thermal model for forecasting the real-time temperature of downhole electronics, Int. J. Therm. Sci. 200 (2024) 108946.
[27] Jiale Peng, Wei Lan, Chao Deng, Fulong Wei, Siqi Ding, Hu Run, Bofeng Shang, Xiaobing Luo, An improved numerical model based on the equivalent thermal conductivity method for downhole thermal management systems, Int. Commun. Heat Mass Transf. 152 (2024) 107317.
[28] Jiale Peng, Wei Lan, Fulong Wei, Chao Deng, Bin Xie, Xiaobing Luo, A numerical model coupling multiple heat transfer modes to develop a passive thermal management system for logging tool, Appl. Therm. Eng. 223 (2023) 120011.
[29] Jiawei Zhang, Wei Lan, Chao Deng, Fulong Wei, Xiaobing Luo, Thermal optimization of high-temperature downhole electronic devices, IEEE Trans. Compon. Packag. Manuf. Technol. 11 (11) (2021) 1816–1823.
[30] Farouq Zitouni, Saad Harous, Integrating the opposition nelder–mead algorithm into the selection phase of the genetic algorithm for enhanced optimization, Appl. Syst. Innov. 6 (5) (2023) 80.
[31] Fulong Wei, Chao Deng, Jiale Peng, Xiaobing Luo, Thermal optimization of a logging tool used in high temperature downhole environment, in: 2022 IEEE International Power Electronics and Application Conference and Exposition (PEAC), IEEE, 2022, pp. 72–77.
[32] Ji Lang, Qianqian Wang, Shan Tong, Investigation of heat source layout optimization by using deep learning surrogate models, ASME J. Heat Mass Transf. 146 (6) (2024).
[33] Zengjia Guo, Yang Wang, Siyuan Zhao, Tianshou Zhao, Meng Ni, Modeling and optimization of micro heat pipe cooling battery thermal management system via deep learning and multi-objective genetic algorithms, Int. J. Heat Mass Transf. 207 (2023) 124024.
[34] Wencan Zhang, Zhicheng Liang, Wu Weixiong, Guozhi Ling, Ruixin Ma, Design and optimization of a hybrid battery thermal management system for electric vehicle based on surrogate model, Int. J. Heat Mass Transf. 174 (2021) 121318.
[35] Khalil Dammak, Abdelkhalak El Hami, Thermal reliability-based design optimization using Kriging model of PCM based pin fin heat sink, Int. J. Heat Mass Transf. 166 (2021) 120745.
[36] Lisheng Ye, Caisheng Li, Changhong Wang, Junxin Zheng, Kaiwei Zhong, Wu Tingting, A multi-objective optimization approach for battery thermal management system based on the combination of BP neural network prediction and NSGA-II algorithm, J. Energy Storage 99 (2024) 113212.
[37] Lixin Wang, Yankong Song, Chao Lyu, Dazhi Yang, Wenting Wang, Structure optimization of the battery thermal management system based on surrogate modeling of approximate and detailed simulations, Appl. Therm. Eng. 235 (2023) 121289.
[38] Wu Ming-yu, Xian-jun He, Xiao-hui Sun, Ting-shuai Tong, Zhi-hua Chen, Chun Zheng, Efficient aerodynamic shape optimization using transfer learning based multi-fidelity deep neural network, Phys. Fluids 36 (11) (2024).
[39] Guannan Li, Liang Chen, Jiangyan Liu, Xi Fang, Comparative study on deep transfer learning strategies for cross-system and cross-operation-condition building energy systems fault diagnosis, Energy 263 (2023) 125943.
[40] Siqi Zhang, Jiale Peng, Chao Deng, Fulong Wei, Jiacheng Li, Jinlong Ma, Xiaobing Luo, An integrated downhole thermal management system with improved operating thermal performance and rapid post-operation air cooling, Appl. Therm. Eng. 257 (2024) 124473.
[41] Piera Di Prima, Michele Santovito, Davide Papurello, CFD analysis of a latent thermal storage system (PCM) for integration with an air-water heat pump, Int. J. Energy Res. 2024 (1) (2024) 6632582.
[42] Chao Deng, Fulong Wei, Wei Lan, Jiale Peng, Xiaobing Luo, Experimental and numerical investigation of low melting point alloy for downhole electronics at high temperature, in: 2022 IEEE International Power Electronics and Application Conference and Exposition (PEAC), IEEE, 2022, pp. 49–54.
[43] L. Di Natale, B. Svetozarevic, P. Heer, Cn Jones, Physically consistent neural networks for building thermal modeling: theory and analysis, Appl. Energy 325 (2022) 119806.